

## Langmuir Circulation: An Agent for Vertical Restratification?

KE LI, ZHEXUAN ZHANG, GREG CHINI, AND GLENN FLIERL

*University of New Hampshire, Durham, New Hampshire*

(Manuscript received 30 November 2011, in final form 7 July 2012)

### ABSTRACT

Comparably little is known about the impact of down-front-propagating surface waves on the stability of submesoscale lateral fronts in the ocean surface mixed layer. In this investigation, the stability of lateral fronts in gradient–wind balance to two-dimensional (down-front invariant) disturbances is analyzed using the stratified, rotating Craik–Leibovich (CL) equations. Through the action of the CL vortex force, the surface waves fundamentally alter the superinertial, two-dimensional linear stability of these fronts, with the classical symmetric instability mode being replaced by a hybrid Langmuir circulation/symmetric mode. The hybrid mode is shown to exhibit much larger growth rates than the pure symmetric mode, to exist in a regime in which the vertical Richardson number is greater than 1, and to accomplish significant cross-isopycnal transport. Nonhydrostatic numerical simulations reveal that the nonlinear evolution of this hybrid instability mode can lead to rapid, that is, superinertial, vertical restratification of the mixed layer. Paradoxically, Langmuir circulation—generally viewed as a prominent vertical mixing mechanism in the upper ocean—may thus play a role in mixed layer restratification.

### 1. Introduction

Lateral density gradients associated with submesoscale fronts are ubiquitous in the ocean surface mixed layer (Samelson and Paulson 1988; Ferrari and Rudnick 2000; Munk et al. 2000). These fronts have a width on the order of one to ten kilometers and are nominally in gradient wind balance; that is, the cross-front gradient in hydrostatic pressure is balanced by Coriolis forces associated with a vertically sheared alongfront current. There has been significant recent interest in understanding frontal instabilities and their role in the consequent restratification of the mixed layer (ML) and in the loss of balance associated with a forward energy cascade. Boccaletti et al. (2007), in particular, demonstrate that a three-dimensional (3D), essentially geostrophic (i.e., balanced) but  $O(1)$  Rossby number baroclinic Eady mode, which they refer to as the mixed layer instability (MLI), causes frontal slumping and restratification on time scales of a few days—much shorter than that associated with mesoscale baroclinic instability. Molemaker et al. (2005) show that a second mode, the ageostrophic

anticyclonic instability (AAI), exhibits a large nonhydrostatic unbalanced component, which may be important for the extraction of kinetic energy residing in ocean mesoscale flows and its ultimate dissipation via small-scale, three-dimensional turbulence.

In addition to these 3D instabilities, lateral fronts, particularly within the ML where the vertical stratification is weak and hence horizontal gradients are comparably strong, are subject to a two-dimensional (2D; down-front invariant) gravitational/centrifugal instability referred to as symmetric instability (Haine and Marshall 1998). Linear inviscid stability analysis in an unbounded domain indicates that the symmetric mode arises for  $0 \leq Ri_v < 1$ , where the vertical Richardson number  $Ri_v = N^2 H^2 / U^2$ ,  $N^2$  is the ML buoyancy frequency,  $H$  is the ML depth, and  $U$  is a velocity scale characterizing the thermal wind (Stone 1970; Hoskins 1974). Under these conditions, along-isopycnal angular momentum gradients trigger centrifugal instabilities that grow on a time scale proportional to the inverse of the Coriolis parameter  $f$ . Fully nonlinear numerical simulations confirm that the mixing accomplished by the symmetric mode continues until  $Ri_v \approx 1$  (Haine and Marshall 1998). Since the most rapidly growing perturbations are aligned with isopycnals, the net result is an efficient but minimal *vertical* restratification of the ML.

*Corresponding author address:* Greg Chini, University of New Hampshire, W113 Kingsbury Hall, Durham, NH 03824.  
E-mail: greg.chini@unh.edu

[Taylor and Ferrari (2009) show that the saturation of the growing symmetric instability can be accomplished by a vertical flux of positive potential vorticity across the thermocline following a secondary Kelvin–Helmholtz instability of the symmetric mode.] Indeed, Boccaletti et al. (2007) argue that the bulk of the restratification occurs via the MLI which ensues after  $Ri_v \geq 1$  and which effectively releases the potential energy in the horizontal stratification.

To date, less attention has been paid to the interaction between lateral density gradients within the ML and smaller-scale convective (vertical) mixing processes that can and do arise independently of the existence of fronts. One notable exception is the recent study by Taylor and Ferrari (2010) of the impact of a geostrophically balanced lateral density gradient on turbulent thermal convection in the upper ocean. Their results suggest that the presence of the density front can modify the structure of the *vertical* stratification and the development of the surface boundary layer.

More significant, perhaps, is the omission in most prior investigations (including those referenced above) of surface wave effects on the stability of ML fronts, which not only precludes the occurrence of Langmuir circulation (LC), a primary vertical mixing mechanism in the ocean surface boundary layer under wind forced seas (Leibovich 1983; McWilliams et al. 1997; Thorpe 2004), but also the modification of other instability processes by the rectified effects of the waves through the action of the Craik–Leibovich (CL) vortex force. Not surprisingly, the focus of nearly all numerical process studies of Langmuir circulation in a density stratified environment—starting with a series of two-dimensional (downwind invariant) numerical simulations by Li and Garrett (Li and Garrett 1995, 1997), and continuing with fully three-dimensional large-eddy simulations (LES) of turbulent Langmuir circulation by, for example, Skillingstad and Denbo (1995); McWilliams et al. (1997); Li et al. (2005)—has been on the effects of an imposed strictly vertically varying density profile on the development of the vortices and the evolution of the surface mixed layer.

Motivated by the routine occurrence of submesoscale fronts in the upper ocean, we here address the role of down-front-propagating surface waves on the evolution of these fronts. Specifically, we simultaneously investigate the influence of an *imposed lateral* density gradient on Langmuir circulation and the effect of the CL vortex force on the classical symmetric instability mode. Note that we do not study the possible two-way coupling between these instability modes and the more slowly evolving processes responsible for maintaining submesoscale fronts—although we view the present

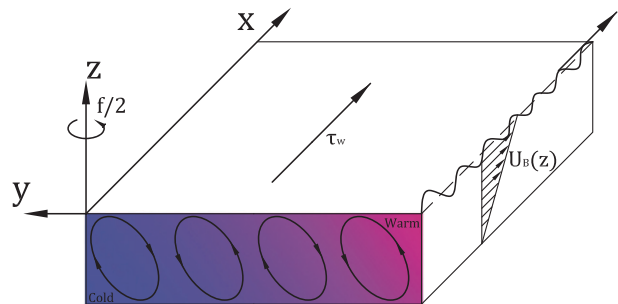


FIG. 1. Schematic of LC roll vortices in the presence of a horizontal density gradient within the mixed layer. The wind (with associated traction  $\tau_w$ ) and surface waves are aligned in the down-front, that is,  $x$ , direction. The imposed lateral density (temperature) gradient is oriented in the positive (negative)  $y$  direction.

investigation as a necessary first step toward addressing the two-way multiscale interaction between fronts and mixed layer turbulence. Instead, our primary aim is to elucidate the nature of the convective instability and the physical mechanisms involved. We consider an idealized scenario in which the dynamics are 2D, with no variation in the alongfront direction, but involve all three velocity components. We also imagine that the LC evolves in a preexisting mixed layer which is “slippery” to the cellular flow and that there exists a sufficiently strong pycnocline to inhibit further layer deepening by the cells over the time scales of interest. Further details of the problem formulation are given in section 2. Using a complement of linear stability theory, energy budgets, and fully nonlinear, nonhydrostatic numerical simulations of the rotating, laterally stratified 2D CL equations (section 3 and section 4, respectively), we diagnose the physics of the fastest growing primary instability mode and its subsequent secondary instability and nonlinear evolution. We conclude in section 5 with a discussion of the potential implications of our results for ML restratification.

## 2. Problem formulation

As shown in Fig. 1, we adopt a Cartesian coordinate system in which the  $x$  axis is aligned with the front and with the presumed direction of both the wind and the vertically varying surface wave Stokes drift velocity  $\mathbf{U}_s = U_s(z)\hat{\mathbf{x}}$ . The vertical coordinate  $z$  measures distance upward from the mean position of the sea surface, and the cross-front coordinate  $y$  is oriented so as to complete a right-handed coordinate system. To explore the dynamics of LC and other phenomena characterized by time scales long compared to the typical surface wave period, we employ the rotating CL equations—a surface wave–filtered version of the incompressible Navier–Stokes equations

(Craig and Leibovich 1976; Leibovich 1977; Craig 1977; Huang 1979; Leibovich 1983; Holm 1996; McWilliams et al. 1997)—on an  $f$  plane (where  $f$  is the Coriolis parameter) and under the Boussinesq approximation, namely,

$$\frac{D\mathbf{U}}{Dt} + f\hat{\mathbf{z}} \times \mathbf{U} = -\frac{1}{\rho_0}\nabla p - \frac{\rho}{\rho_0}g\hat{\mathbf{z}} + \nu_e\nabla^2\mathbf{U} + \mathbf{U}_s \times (f\hat{\mathbf{z}} + \nabla \times \mathbf{U}). \quad (1)$$

Here,  $\rho$  is the density field, with  $\rho_0$  a constant representative value;  $\mathbf{U} = (U, V, W)$  is the incompressible velocity field;  $p$  is a modified pressure;  $g$  is the gravitational acceleration; and  $\nu_e$  is the presumed constant eddy viscosity that arises from the Craig–Leibovich wave-filtering procedure. The substantial derivative operator  $D/Dt = \partial/\partial t + \mathbf{U} \cdot \nabla$ , where  $t$  is the time variable. The final term on the right-hand side of (1) consists of the Stokes–Coriolis force (McWilliams et al. 1997; Lewis and Belcher 2004) and the CL vortex force, the cross-product of the Stokes drift velocity associated with the filtered surface waves—a prescribed input in this formalism—and the (time or phase averaged) relative vorticity vector.

Numerous prior studies have shown that the dominant (i.e., fastest growing, most energetic) instability modes take the form of  $x$  invariant roll vortices, or “Langmuir cells,” when the wind and waves are aligned in the  $x$  direction. We presume this to be the case even when lateral stratification and Coriolis forces are incorporated and henceforth restrict attention to  $x$  invariant dynamics (although we allow for flow in the  $x$  direction). To nondimensionalize the governing equations, we choose the mixed layer depth  $H$  to be the relevant length scale. Attributing density variations entirely to temperature anomalies, and assuming a linear equation of state relating density  $\rho$  to the temperature  $T$ , we scale temperature by

$$\Delta T \equiv \left. \frac{dT_f}{dy} \right|_H \equiv \left( \frac{1}{\alpha g} M^2 \right) H, \quad (2)$$

roughly the temperature difference across a typical Langmuir cell. In (2),  $T_f(y)$  is the imposed, linear lateral stratification (with constant gradient  $dT_f/dy$ ),  $\alpha$  is the coefficient of thermal expansion of seawater, and  $M$  is, thus, the Brunt frequency associated with the horizontal density gradient. The typical alongfront flow speed  $\mathcal{U} = O(M^2 H/f)$  is then used to scale all velocity components except for the Stokes drift velocity, which is scaled with  $U_{s0} = U_s(0)$ . The time variable is nondimensionalized by the convective or eddy-turnover time scale  $H/\mathcal{U}$ .

Using these scalings, the nondimensional, downwind-invariant, stratified, rotating CL equations can be cast in a streamfunction vorticity form:

$$U_t + \psi_z U_y - \psi_y U_z = \text{Ro}^{-1} \psi_z + \text{La} \nabla^2 U, \quad (3)$$

$$\Omega_t + \psi_z \Omega_y - \psi_y \Omega_z = \text{Ri}_h T_y + \text{Ro}^{-1} [U_z + S U'_s(z)] - S U'_s(z) U_y + \text{La} \nabla^2 \Omega, \quad (4)$$

$$\nabla^2 \psi = -\Omega, \quad \text{and} \quad (5)$$

$$T_t + \psi_z T_y - \psi_y T_z = \text{Pe}^{-1} \nabla^2 T. \quad (6)$$

In (3)–(6), all variables are now *nondimensional* and subscripts denote partial differentiation. Here,  $\Omega$  is the  $x$  vorticity component, and  $\psi$  is the associated streamfunction, with  $V = \psi_z \equiv v$  and  $W = -\psi_y \equiv w$ . For analytical simplicity, we take the Stokes drift to be a linear rather than more realistic exponentially decaying function of depth,  $U_s(z) = z + 1$ , where we set the Stokes parameter  $S \equiv U_{s0}/\mathcal{U}$  to unity or zero to incorporate or exclude surface wave effects, respectively. Note that, even with wave effects included, there is no temperature advection by the Stokes drift owing to the assumption of streamwise invariance. Five other nondimensional parameters appear in these equations: the laminar Langmuir number  $\text{La} \equiv \nu_e/(\mathcal{U}H)$ , which can be interpreted as an inverse Reynolds number; the Peclet number  $\text{Pe} \equiv \mathcal{U}H/\kappa_e$ , where  $\kappa_e$  is an eddy diffusivity for heat; the ML Rossby number  $\text{Ro} = \mathcal{U}/(fH)$ ; and the *horizontal* Richardson number  $\text{Ri}_h \equiv M^2/(\mathcal{U}H)^2$ .

To complete the problem specification, (3)–(6) are supplemented by appropriate dimensionless boundary conditions at the mean position of the free surface  $z = 0$  and along the mixed layer base  $z = -1$ :

$$U_z = 1, \quad \Omega = 0, \quad \psi = 0, \quad T_z = \gamma, \quad (7)$$

where the ratio of the square of the vertical to horizontal buoyancy frequency  $\gamma = N^2/M^2$ . Following Taylor and Ferrari (2009), we have specifically chosen the momentum and heat flux boundary conditions in (7) to minimize the effects of dynamic buoyancy forcing via Ekman drift (Thomas and Ferrari 2008) and to allow for a base state with linear vertical and lateral thermal stratification. Indeed, (3)–(6) and boundary conditions (7) admit a unidirectional base flow

$$U_B(z) = z + U_{B_0} \quad (8)$$

that is in surface-wave-modified gradient wind balance with an imposed basic-state temperature distribution

$$T_B(y, z) = \gamma z - y + T_{B_0}, \quad (9)$$

for constants  $U_{B_0}$  and  $T_{B_0}$ , provided that  $\text{RoRi}_h = 1 + S$ . In dimensional terms, this last condition can be expressed as  $\alpha g(\Delta T/H)dT_B/dy = -f(U/H)(dU_B/dz + SdU_s/dz)$ ; that is, the usual gradient wind balance condition modified by the Stokes–Coriolis torque. Strictly speaking, it is inappropriate to refer to this base state as a front, of course, since (8) has no horizontal structure. In this study, we nevertheless continue to use this terminology (again following, e.g., Taylor and Ferrari (2009)) but with the understanding that we are modeling a  $L = O(1)$  km wide section of a lateral front encompassing tens of Langmuir cells and across which the temperature field may reasonably be approximated as linearly varying. Except for the total temperature  $T$ , all fields are taken to be  $L$ -periodic in the  $y$  coordinate.

The traction boundary condition  $U_z = 1$  in (7) ensures that the imposed down-front wind stress *exactly* cancels the so-called geostrophic stress (Thomas and Rhines 2002), eliminating the possibility of a residual Ekman drift. As discussed in Thomas and Ferrari (2008), down-front winds driving a dimensional frictional surface shear  $u_*^2/\nu_e$  greater than the geostrophic shear  $U/H$  ( $=M^2/f$  in the absence of the Stokes–Coriolis force) will induce an Ekman drift that tends to destratify the mixed layer by advecting heavy fluid over light; conversely, down-front winds driving a frictional surface shear less than the geostrophic shear will induce an Ekman drift that drives vertical restratification. Given our nondimensionalization, the implied water friction velocity  $u_* = O(0.005)$  m s<sup>-1</sup>, using  $U = 0.1$  m s<sup>-1</sup> and  $H = 50$  m as representative values. When  $S = 1$ , these winds and waves are appropriate for the dynamical regime identified as “Langmuir turbulence” by McWilliams et al. (1997).

In what follows, we take  $\gamma \geq 0$  and consider the linear and nonlinear stability of the imposed front to down-front invariant disturbances. We fix  $\text{La}$  and  $\text{Pe}$  at moderately small and large values, respectively, and treat  $\text{Ri}_h$  and  $\text{Ri}_v \equiv \gamma\text{Ri}_h$ , the vertical Richardson number, as the key control parameters.

### 3. Linear stability analysis

To gain insight into the convective structures likely to emerge from the base state described in section 2, we first perform a linear stability analysis. Decomposing the  $x$  velocity component and the temperature into basic-state (denoted with “ $B$ ” subscripts) and perturbation contributions,  $U = U_B + u$  and  $T = T_B + \theta$ , and linearizing the dynamics about this basic state gives the (linearized) equations governing the evolution of the perturbations:

$$u_t = \psi_y + \text{Ro}^{-1}\psi_z + \text{La}(u_{yy} + u_{zz}), \quad (10)$$

$$\Omega_t = \text{Ri}_h\theta_y + \text{Ro}^{-1}u_z - Su_y + \text{La}(\Omega_{yy} + \Omega_{zz}), \quad (11)$$

$$\nabla^2\psi = -\Omega, \quad \text{and} \quad (12)$$

$$\theta_t = \gamma\psi_y + \psi_z + \text{Pe}^{-1}(\theta_{yy} + \theta_{zz}). \quad (13)$$

The perturbation fields are  $L$  periodic in the  $y$  coordinate and satisfy homogeneous boundary conditions along  $z = 0$  and  $z = -1$ :

$$u_z = 0, \quad \Omega = 0, \quad \psi = 0, \quad \theta_z = 0. \quad (14)$$

Decomposing the generic perturbation field

$$\phi(y, z, t) = \hat{\phi}(z)e^{iky}e^{\sigma t} + \text{c.c.} \quad (15)$$

and substituting into (10)–(14) yields an ordinary differential eigenvalue problem in  $z$  for each horizontal wavenumber  $k$ , where  $\hat{\phi}(z)$  and  $\sigma$  are the (generally complex) vertical eigenfunction and eigenvalue.

With the given boundary conditions, the complete linear stability problem must be solved numerically (see below), but the instability physics can be largely understood by performing a nondissipative stability analysis (for which  $\text{La} = \text{Pe}^{-1} = 0$ ) in a vertically unbounded domain, so that  $\hat{\phi}(z) = e^{imz}$  in (15). Under these simplifications,  $\sigma$  depends only on the ratio  $\lambda = -m/k$  rather than on  $k$  and  $m$  separately. An analytical expression for  $\sigma$  is readily found to be given by

$$(1 + \lambda^2)\sigma^2 = -\text{Ro}^{-2} + (\text{Ro}^{-1} + \text{Ri}_h - S\text{Ro}^{-1})\lambda - (\text{Ri}_v - S)\lambda^2, \quad (16)$$

where in the absence of waves  $S = 0$  and  $\text{Ro}^{-1} = \text{Ri}_h$  while in the presence of waves  $S = 1$  and  $\text{Ro}^{-1} = \text{Ri}_h/2$ . It is instructive to consider various limiting cases of (16) representing distinct and hybridized modes of linear instability; see Table 1 for a taxonomy of these various instability modes.

As suggested in Fig. 2, in the absence of surface waves, vertical stratification within the ML, and Coriolis accelerations [case (i)], counterrotating cellular disturbances inclined at 45 degrees to the vertical in the direction of the density gradient are most efficiently able to release the potential energy stored in the lateral front by moving less dense fluid above more dense fluid. In addition to this purely buoyancy-driven instability mechanism, which leads to inclined convection cells, inertial instability is possible when Coriolis accelerations are incorporated, even in the absence of density stratification [case (ii)].

TABLE 1. Taxonomy of 2D (down-front invariant) linear instability modes of the base state (8)–(9) modeling the central region of a submesoscale lateral front in the surface ML. Note that in case (i), Coriolis accelerations are (artificially) suppressed (i.e.,  $\text{Ro}^{-1} = 0$  but  $\text{Ri}_h$  is finite), while in case (ii), lateral density gradients are suppressed (i.e.,  $\text{Ri}_h = 0$  but  $\text{Ro}^{-1}$  is finite). In scenarios (iii) and (iv),  $\text{Ro}^{-1} = \text{Ri}_h$  and in case (v),  $\text{Ro}^{-1} = \text{Ri}_h/2$ . The subscript “*f*” refers to a property of the fastest-growing linear mode. (Concise analytical forms for certain properties have been obtained by taking representative asymptotic limits.)

Case	Instability mode	$S$	$\text{Ri}_v$	$\lambda_f$	$\sigma_f$
i	Buoyancy driven	0	0	1	$\sqrt{\text{Ri}_h/2}$
ii	Inertial	0	0	1	$\sqrt{\text{Ro}^{-1}/2}$
iii	“Pure” symmetric	0	0	1	$\sqrt{\text{Ri}_h}$
iv	“Classical” symmetric	0	$\gg \text{Ri}_h$	$M^2/N^2$	$\sqrt{\text{Ri}_h^2/\text{Ri}_v - \text{Ri}_h^2}$
v	Hybrid LC/symmetric	1	1	1	$\sqrt{\text{Ri}_h/2}$

Specifically, vertical gradients in the perturbation down-front velocity component  $u$  tilt vertical planetary vorticity filaments into the  $x$  direction, creating counterrotating cellular disturbances. Energy stored in the down-front basic-state shear flow is extracted by the cellular flow; in terms of momentum fluxes, the rate at which down-front momentum near the surface is advected into the convergence zones between the cells exceeds the rate at which momentum is extracted near the ML base. Interpreted in this way, this form of inertial instability is loosely analogous to the CL2 mechanism responsible for Langmuir circulation, except that 1) in LC, the imposed surface wave Stokes drift tilts vertical vorticity associated with spanwise-varying streamwise velocity perturbations into the streamwise direction, while in the inertial instability, vertical gradients in the streamwise velocity perturbations tilt the imposed vertical planetary vorticity filaments into the streamwise direction (as noted above); and 2) the fastest-growing inertial modes are inclined at 45 degrees to the vertical because the imposed planetary vorticity is of one sign unlike the perturbation vertical vorticity field in the LC case.

In pure symmetric instability (i.e., in the absence of surface waves), the buoyancy and vortex-tilting mechanisms are both operative and contribute equally to the growth rate of the disturbance, which is approximately equal to the square root of the horizontal Richardson number [case (iii)]. In what may be termed “classical symmetric instability” [case (iv)], stabilizing residual vertical stratification within the mixed layer (which often is stronger than the lateral stratification there) significantly reduces growth rates; in fact, the idealized analysis suggests that classical symmetric instability is completely inhibited when  $\text{Ri}_v \geq 1$ , a result that full numerical simulations confirm persists into the nonlinear regime. Moreover, the streamlines of the fastest growing classical symmetric modes are roughly parallel to isopycnal surfaces (since the fastest growing mode has a wavenumber ratio satisfying  $\lambda_f \approx M^2/N^2$ ), implying that symmetric instability accomplishes little cross-isopycnal

transport. All these results are consistent with previous analyses; see, for example, Hoskins (1974), Haine and Marshall (1998), and Taylor and Ferrari (2009).

Remarkably, the linear analysis suggests that in the presence of down-front-propagating surface waves [case (v)] the fastest growing modes again are inclined at 45 degrees to the vertical, implying significant cross-isopycnal transport and greatly enhanced growth rates relative to classic symmetric instability. Indeed, for  $\text{Ri}_v = 1$ , a regime in which the classical symmetric mode is suppressed, the properties of the fastest growing mode essentially accord with those for the scenario in which *neither* surface waves nor vertical stratification is present [case (iii)]. Heuristically, the fastest growing disturbance in case (v) is a hybrid LC/symmetric mode that is able to exploit multiple instability mechanisms for enhanced growth, with, for example, the destabilizing CL vortex torque neutralizing the stabilizing buoyancy torque associated with vertical stratification.

The predictions of the idealized analysis are broadly confirmed (albeit refined) by a full linear stability analysis in which the effects of vertical boundaries and diffusion are retained. We solve the full problem using a Chebyshev spectral collocation method (Trefethen 2000)

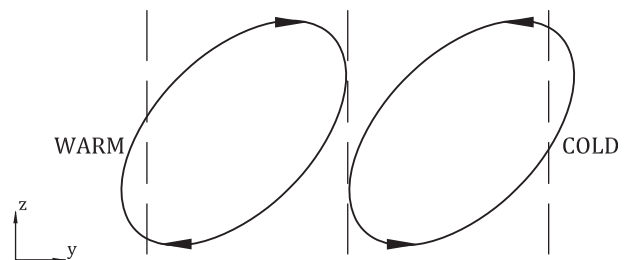
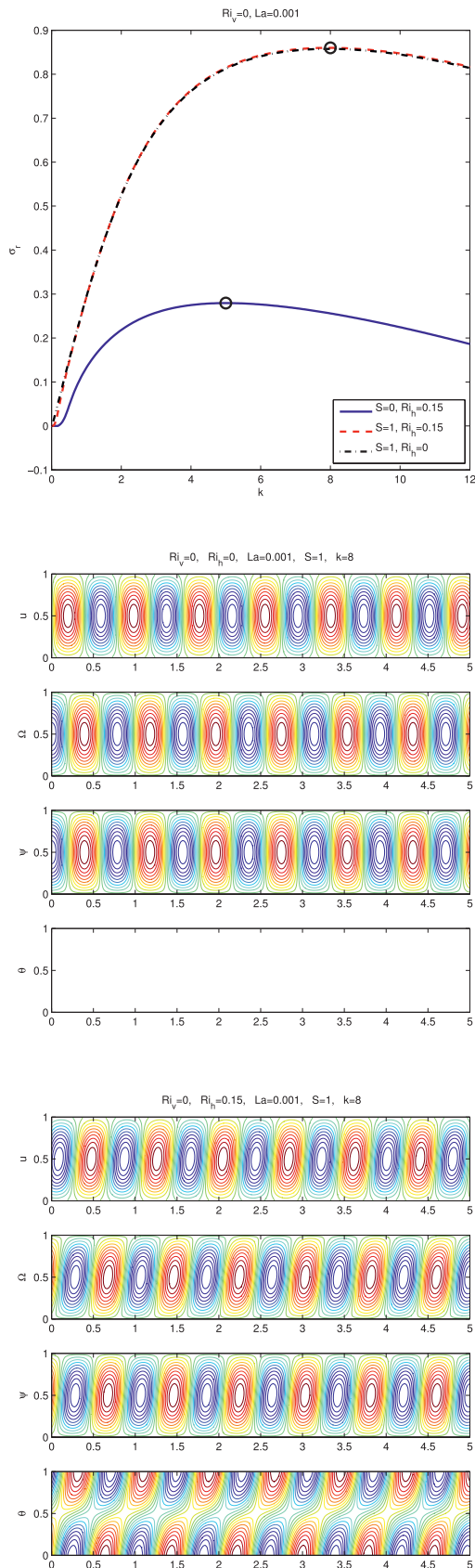


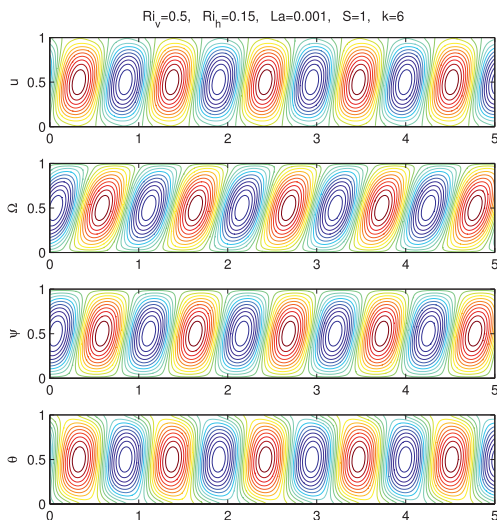
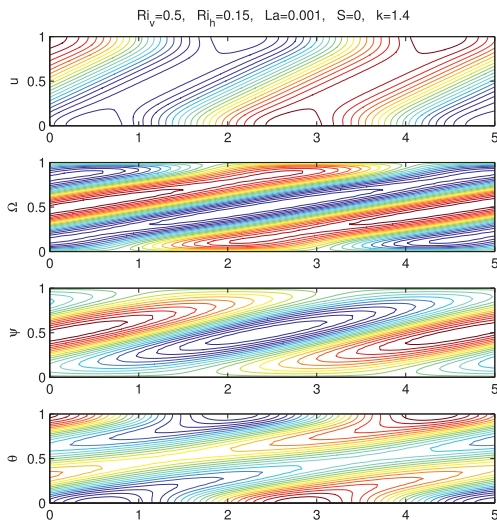
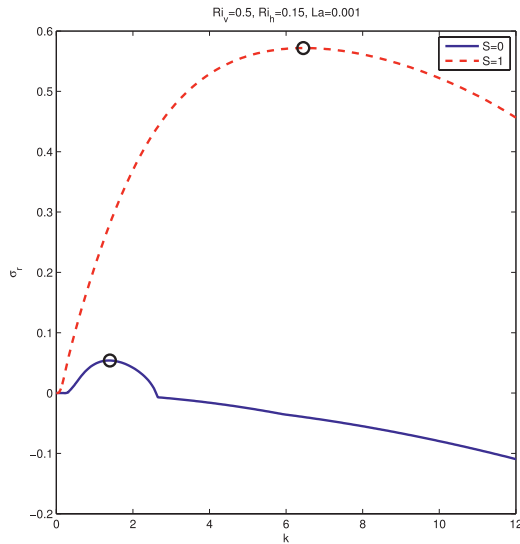
FIG. 2. Schematic illustrating a buoyancy-driven mechanism for instability in the presence of an imposed, strictly horizontal density gradient. Counterrotating cellular disturbances inclined in the direction of the density gradient (i.e., in the positive  $y$  direction) tend to move warm fluid above cold fluid, thereby releasing potential energy stored in the lateral density front.



with 40–50 modes. Figures 3, 4, and 5 show the real part of the growth rate of the fastest growing instability mode for  $Ri_v = 0, 0.5,$  and  $1,$  respectively, for a modest value of  $Ri_h = 0.15,$  both without (lower curves) and with (upper curves) surface wave effects. In these and all of the following results discussed below,  $La = 0.001$  and  $Pe = 4000.$  For all parameter values considered, it is clear that surface wave effects enhance, in some cases by almost an order of magnitude, the growth rate of the dominant instability mode. As expected, growth rates are reduced as  $Ri_v$  is increased, although much more so for the symmetric than for the hybrid mode. Notably, the full stability calculations confirm that the hybrid mode can exist in a parameter regime ( $Ri_v \geq 1$ ) in which the symmetric mode is completely suppressed (see Fig. 5).

Also depicted in Figs. 3–5 are the eigenfunctions corresponding to the fastest-growing perturbation fields. Although the upper plot in Fig. 3 indicates that in the presence of surface waves growth rates are essentially unchanged by lateral stratification (cf. the red and black curves), the eigenfunction plots clearly reveal that the Langmuir cells nevertheless feel the influence of the lateral front by inclining to the vertical in the direction of increasing density to extract potential energy stored in the front, as anticipated. As described in section 4, this *cell tilting* has a crucial effect on the subsequent *non-linear evolution* of the disturbance and, ultimately, on the stratification within the ML. Figure 4 confirms that, in the presence of stabilizing vertical stratification, the fastest-growing classical symmetric instability mode has streamlines that are roughly parallel to the basic-state isopycnals (middle plots), while the fastest-growing hybrid mode evidently can accomplish cross-isopycnal transport (bottom plots). Finally, for  $Ri_v = 1,$  two hybrid modes appear with comparable maximum growth rates (see Fig. 5). Unlike the hybrid modes at smaller values of  $Ri_v,$  the high wavenumber hybrid mode at  $Ri_v = 1$  shown in the bottom plots in Fig. 5 is a traveling instability. The lower wavenumber mode, which turns out to play a more

←  
 FIG. 3. Instability growth rates and eigenfunctions for  $Ri_v = 0,$   $Ri_h = 0.15,$   $La = 0.001,$  and  $Pe = 4000.$  (top) Real part of the growth rate  $\sigma_r$  of the fastest-growing disturbance vs disturbance wavenumber  $k$  both with (dashed curve,  $S = 1$ ) and without (solid curve,  $S = 0$ ) surface wave effects. For reference, the dashed-dotted curve (overlying the dashed,  $S = 1$  curve) corresponds to the case in which there is no density stratification (i.e.,  $Ri_h = Ri_v = 0$ ) and Coriolis accelerations are suppressed ( $Ro \rightarrow \infty$ ); that is, the canonical Langmuir circulation scenario. (bottom) 2D maximally-growing perturbation eigenfunctions ( $u, \Omega, \psi, \theta$ ) for  $S = 1$  both without (middle) and with (bottom) lateral stratification.



important role in the nonlinear evolution of the ML stratification, is stationary.

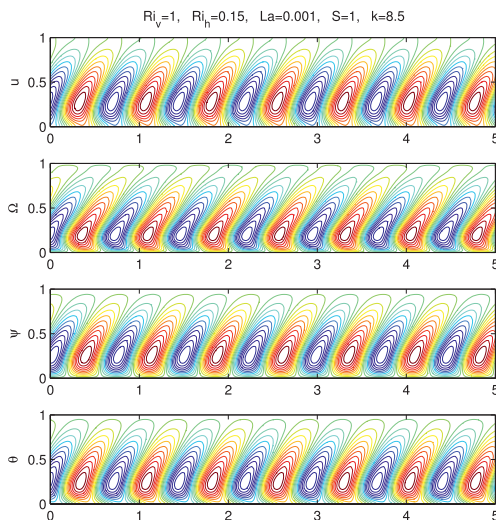
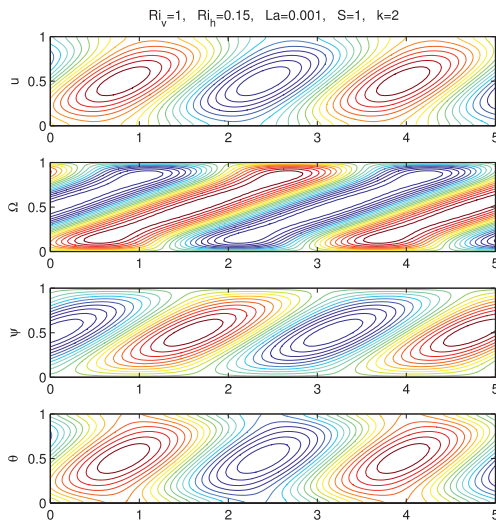
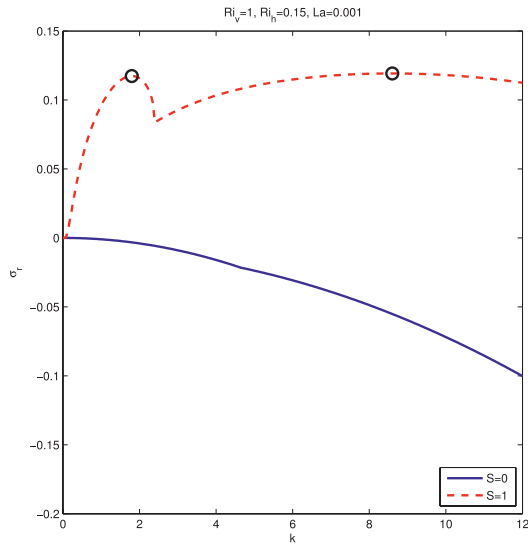
#### 4. Nonlinear simulation of hybrid LC/symmetric instability

Next, we investigate the finite-amplitude evolution of the hybrid LC/symmetric linear instability, as well as its impact on ML restratification, by numerically integrating the fully nonlinear system (3)–(6) subject to boundary conditions (7). For this purpose, we modified an existing, thoroughly validated pseudospectral code, developed in-house, for solving the 2D (nonhydrostatic) CL equations by incorporating Coriolis accelerations and horizontal and vertical density stratification through the Boussinesq approximation. A Fourier–Chebyshev-tau spatial discretization scheme was employed, and the discretized system was time advanced using a semi-implicit Crank–Nicolson/Adams–Bashforth algorithm. The simulations were initialized with the base profiles (8) and (9) plus a small-amplitude disturbance having the wavenumber of the fastest-growing mode predicted by the full linear stability calculations for the given parameters.

We report the results of three sets of simulations, each for  $La = 0.001$ ,  $Pe = 4000$ ,  $S = 1$ , and  $Ri_h = 0.15$ . Note that this  $La$  corresponds to an eddy viscosity  $\nu_e = La\mathcal{M}H = O(10^{-3})$  for a reasonable range of  $\mathcal{U}$  and  $H$ , in agreement with the *sub-grid-scale*—that is, excluding the effects of LC—viscosity numerically computed in the LES of Langmuir turbulence by McWilliams et al. (1997). Our three simulations are distinguished by  $Ri_v$ , a measure of the *initial* vertical stratification within the ML. In the first case,  $Ri_v = 0$ ; in the second,  $Ri_v = 0.5$ ; and in the third,  $Ri_v = 1$ . The panels in Figs. 6, 7, and 8 depict snapshots of the total fields ( $U, \Omega, \psi$ , and  $T$ , from top to bottom) at four different instants (with time increasing from left to right) during the evolution of the instability. In each case, the dynamics is broadly similar: a hybrid LC/symmetric instability mode, inclined to the vertical, is excited. As this instability is amplified, the cells become asymmetric and their inclination angle oscillates. After several convective time units, a cross-front

←

FIG. 4. Instability growth rates and eigenfunctions for  $Ri_v = 0.5$ ,  $Ri_h = 0.15$ ,  $La = 0.001$ , and  $Pe = 4000$ . (top) Real part of the growth rate  $\sigma_r$  of the fastest-growing disturbance vs disturbance wavenumber  $k$  both with (dashed curve,  $S = 1$ ) and without (solid curve,  $S = 0$ ) surface wave effects. The 2D maximally growing perturbation eigenfunctions ( $u, \Omega, \psi, \theta$ ) for (middle)  $S = 0$  and (bottom)  $S = 1$ .



shear flow is induced, driving light fluid over heavy fluid. The result of this sequence of events is a remarkably efficient, although time-dependent, vertical restratification of the ML—that is, there is an evident oscillation in the mean isopycnal slope following the time of maximum restratification, as can be more readily inferred from the time traces in Fig. 9 and, especially, in Fig. 10 and as discussed in more detail subsequently.

For  $Ri_v = 0$ , the maximum mean vertical stratification, as measured by the nondimensional Brunt frequency squared,  $N_{\max}^2 \equiv t \max [Ri_h(\overline{T}|_{z=0} - \overline{T}|_{z=-1})]$ , where an overbar denotes a horizontal average, occurs at roughly 40 time units; see the third set of panels in Fig. 6. For a 100 m deep ML and a characteristic thermal wind speed of  $0.1 \text{ m s}^{-1}$ , this corresponds to just over 10 h; i.e., very fast restratification. For a range of scenarios, both with and without surface waves, Table 2 quantifies the value of the first maximum in the mean vertical stratification and the time at which that maximum is achieved; the value ( $N_{\min}^2$ ) and time of the first minimum in the vertical stratification *after* the first maximum is also listed. Clearly, for the parameter regime investigated, the hybrid mode is far more effective (roughly a factor of four in terms of  $N_{\max}^2$  for  $Ri_v = 0$  and  $Ri_v = 0.5$ ) than the pure symmetric mode at restratifying the ML, and, again, is operative in a regime  $Ri_v \geq 1$  in which classical symmetric instability is not.

For completeness, we have also tabulated two additional indicators of the impact of the finite-amplitude instability (see Table 3):

$$(\Delta \overline{U})_{\min}^2 \equiv t \min [(\overline{U}|_{z=0} - \overline{U}|_{z=-1})^2]$$

and

$$Ri_{v,\max} \equiv t \max [Ri_h(\overline{T}|_{z=0} - \overline{T}|_{z=-1})(\overline{U}|_{z=0} - \overline{U}|_{z=-1})^{-2}].$$

The former is a measure of the homogenizing effect of the cellular instabilities on the horizontally averaged down-front geostrophic shear, while the latter is the maximum bulk Richardson number, using this characterization of the mean shear. These metrics, too, indicate

←

FIG. 5. Instability growth rates and eigenfunctions for  $Ri_v = 1$ ,  $Ri_h = 0.15$ ,  $La = 0.001$ , and  $Pe = 4000$ . (top) Real part of the growth rate  $\sigma_r$  of the fastest-growing disturbance vs disturbance wavenumber  $k$  both with (dashed curve,  $S = 1$ ) and without (solid curve,  $S = 0$ ) surface wave effects. The 2D maximally growing perturbation eigenfunctions ( $u, \Omega, \psi, \theta$ ) for  $S = 1$  and (middle)  $k \approx 2$  (stationary mode) and (bottom)  $k \approx 8.5$  (traveling mode).

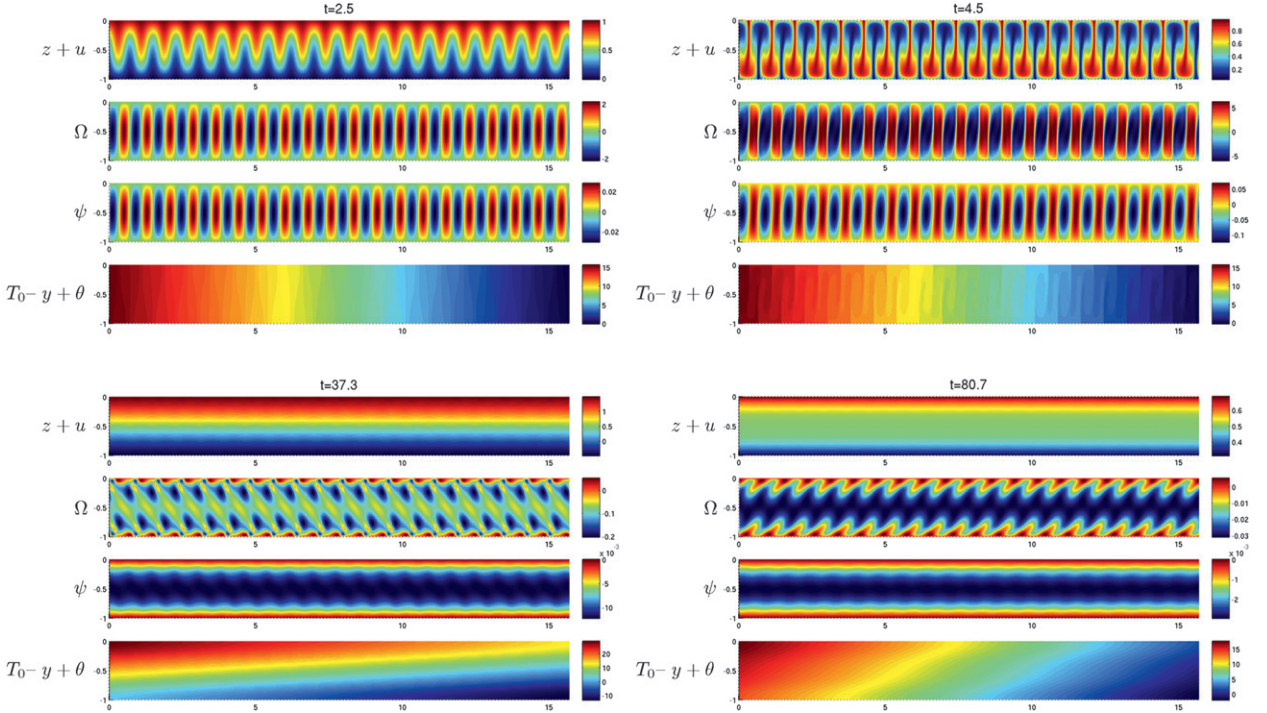


FIG. 6. Snapshots of fully nonlinear numerical simulations for  $Ri_b = 0$ ,  $Ri_n = 0.15$ ,  $S = 1$ ,  $La = 0.001$ , and  $Pe = 4000$ . Plotted in each set of four panels, from top to bottom, is the total down-front velocity  $U$ , the down-front vorticity  $\Omega$ , the streamfunction  $\psi$ , and the total temperature field  $T$ .

that the hybrid mode is a more potent 2D instability of submesoscale lateral fronts than is classical symmetric instability. For example, the hybrid mode can dramatically (albeit transiently) reduce the shear of the base “thermal wind” even for  $Ri_v \geq 0.5$ , while the symmetric mode cannot. (In fact, the hybrid mode can effectively reduce the mean shear to zero during the initial development of the linear instability, which in turn yields a very large  $Ri_{v_{\max}}$ ; for this reason, the tabulated shear values exclude the early time, exponential growth phase of the linear instability.) We note that the maximum values of the vertical Richardson numbers are tempered somewhat by the oscillatory nature of the restratification process, for reasons described in more detail below.

To gain insight into the linear and nonlinear mechanisms driving the time-dependent restratification accomplished by the hybrid LC/symmetric instability mode, it is helpful to examine an energy budget for the fully nonlinear perturbation fields. This budget is derived in the usual way; namely, we multiply the fully nonlinear versions of (10), (11), and (13), that is, with nonlinear (i.e., advection) perturbation terms included, by  $u$ ,  $\psi$ , and  $-\text{Ri}_h\theta$ , respectively, and integrate over the domain. In this way, we obtain, for example, the equation governing the evolution of the down-front perturbation kinetic energy (per unit mass),

$$\text{KE}'_{\parallel} \equiv \langle u^2/2 \rangle,$$

where

$$\langle (\cdot) \rangle \equiv \frac{1}{L} \int_{-1}^0 \int_0^L (\cdot) dy dz$$

and  $L = 2\pi/k$  is the width of the domain:

$$\frac{d\text{KE}'_{\parallel}}{dt} = P_U - C - D'_{\parallel}. \quad (17)$$

Here,  $P_U = -\langle uw dU_B/dz \rangle$  accounts for the production of  $\text{KE}'_{\parallel}$  by the down-front Reynolds stress,  $C \equiv -\text{Ro}^{-1} \langle uw \rangle$  represents energy transfers from down-front to cross-front flows by Coriolis forces, and  $D'_{\parallel} = \text{La} \langle |\nabla u|^2 \rangle$  is the viscous dissipation of  $\text{KE}'_{\parallel}$ . The evolution of the cross-front perturbation kinetic energy (per unit mass),

$$\text{KE}'_{\perp} \equiv \langle (v^2 + w^2)/2 \rangle$$

is governed by

$$\frac{d\text{KE}'_{\perp}}{dt} = P_S + B + C - D'_{\perp}, \quad (18)$$

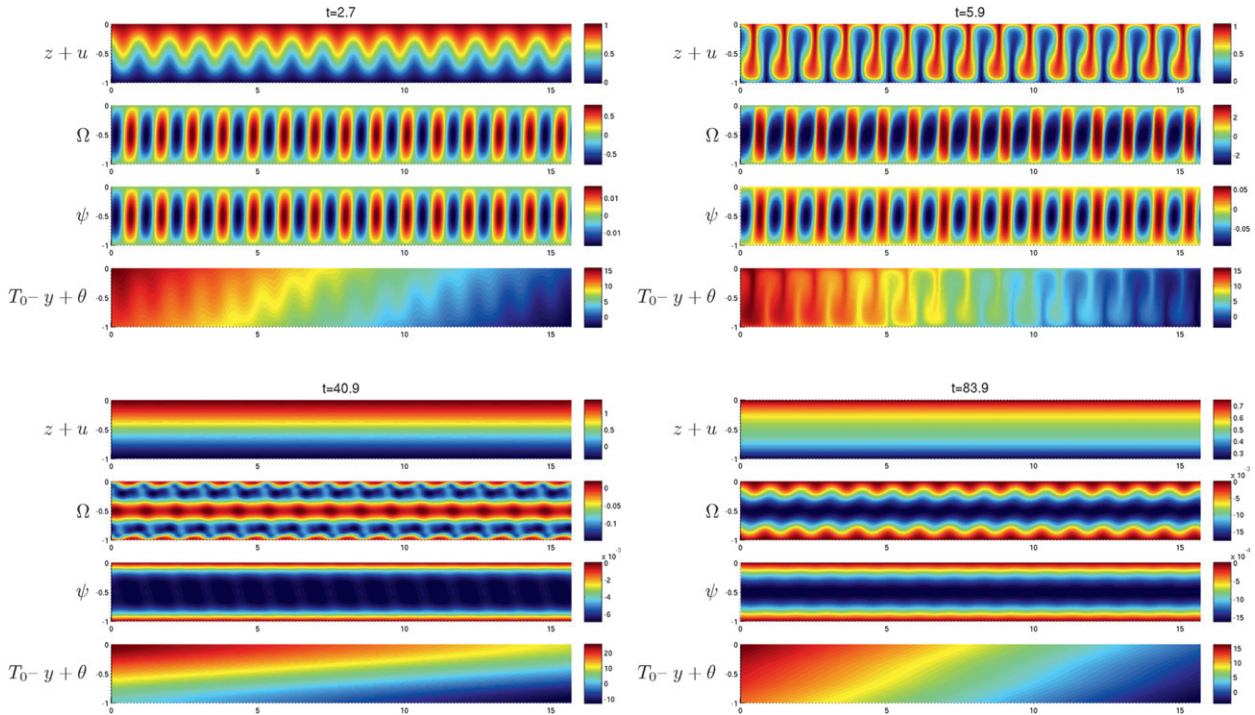


FIG. 7. Snapshots of fully nonlinear numerical simulations for  $Ri_b = 0.5$ ,  $Ri_h = 0.15$ ,  $S = 1$ ,  $La = 0.001$ , and  $Pe = 4000$ . Plotted in each set of four panels, from top to bottom, is the total down-front velocity  $U$ , the down-front vorticity  $\Omega$ , the streamfunction  $\psi$ , and the total temperature field  $T$ .

where the various terms on the right-hand side are defined in Table 4. Finally, the evolution equation for the perturbation potential energy (per unit mass)  $PE' = -Ri_h \langle z\theta \rangle$  is

$$\frac{dPE'}{dt} = -B + Ri_h \int_{-1}^0 z \bar{v} dz + \frac{Ri_h}{Pe} \int_{-1}^0 \frac{\partial \bar{\theta}}{\partial z} dz, \quad (19)$$

where the overbar refers to a  $y$  average. Note that  $PE'$  is one metric for restratification: specifically, the layer is restratifying when  $PE' < 0$ . Considering the first term on the right-hand side of (19), we observe that when  $w$  and  $\theta$  are positively correlated, as in Fig. 2, potential energy is released from the background lateral density gradient and converted to cross-front kinetic energy. The remaining terms vanish for *linear* disturbances ( $v$ ,  $\theta$ ), which necessarily have zero horizontal average; that is, for small-amplitude disturbances, buoyancy production  $B$  is the only factor that can alter the perturbation potential energy. However, during the nonlinear phase of the disturbance evolution, the potential energy may be altered by the last two terms in (19). Of these, the term involving advection of the background potential energy by horizontally averaged cross-front currents is the more important, since  $Pe^{-1} \ll 1$ .

The time evolution of a subset of the various terms in the perturbation energy equations is shown in the series of plots in Fig. 9, which were taken from the simulations depicted in Figs. 6–8. Careful inspection of these energetics along with insights gleaned from the linear stability analysis suggests the following restratification mechanism.

- (i) Linear instability: Hybrid LC/symmetric counter-rotating cellular disturbances *incline* to the vertical, in the direction of the density gradient, to exploit buoyancy production (i.e., to maximize positive or minimize negative  $B$ ).
- (ii) Nonlinear evolution: A “self-self” interaction of the dominant linear mode generates a nonzero  $\overline{v'w'}$  Reynolds stress (RS), since for tilted cells,  $v'$  and  $w'$  (where the primes refer to fluctuations about the horizontal mean) are correlated.
- (iii) Mean flow generation: The vertical divergence of this RS drives a horizontally averaged, vertically sheared cross-front mean flow:

$$\bar{v}_t - \dots = -(\overline{v'w'})_z + \dots$$

- (iv) Mean flow advection: The sign of the induced shear is such that light fluid is carried over heavy fluid,

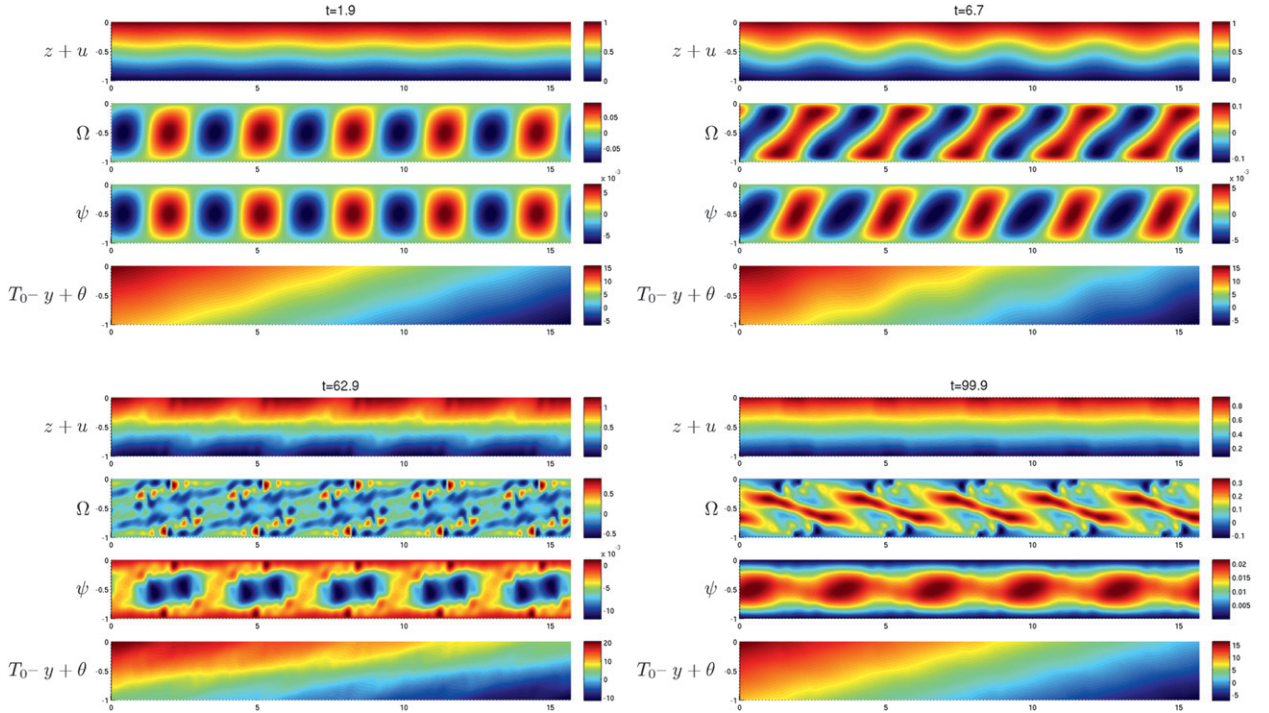


FIG. 8. Snapshots of fully nonlinear numerical simulations for  $Ri_v = 1$ ,  $Ri_h = 0.15$ ,  $S = 1$ ,  $La = 0.001$ , and  $Pe = 4000$ . Plotted in each set of four panels, from top to bottom, is the total down-front velocity  $U$ , the down-front vorticity  $\Omega$ , the streamfunction  $\psi$ , and the total temperature field  $T$ .

restratifying the ML and, owing to the combined influence of cross-cellular shear and increased vertical stratification, shutting down the convection.

- (v) Inertial oscillation: Coriolis forces imply that a nonzero  $\bar{v}$  will induce a nonzero  $\bar{u}$ , since

$$\bar{u}_t - \frac{1}{Ro} \bar{v} = -(\overline{u'w'})_z + La \bar{u}_{zz},$$

$$\bar{v}_t + \frac{1}{Ro} \bar{u} = -(\overline{v'w'})_z + La \bar{v}_{zz}.$$

For small  $La$  and weak or nonexistent convection, an inertial oscillation ensues.

The high-frequency content evident in the energy evolution plots seems to be associated with an *asymmetry* in each pair of counterrotating cells that, itself, is caused by the induced cross-front mean flow. Asymmetry in the structure of a given cell pair implies an asymmetry in the buoyancy and vortex torques experienced by the cells, which evidently tends to right the tilted cells (see, e.g., the second set of panels in Fig. 6). In contrast, the low-frequency part of the signal appears to be the manifestation of a simple inertial oscillation, driven by the action of the Coriolis force on the induced shear flow and having an  $O(Ro^{-1})$  frequency. The phase relationships inherent

in this oscillation are such that  $N^2$  is maximum approximately when  $\bar{v} \approx 0$ , at which time  $(\Delta \bar{U})^2$  is also *maximum*; this phase relationship thus limits the maximum achievable  $Ri_v$ . For this reason,  $N_{\max}^2$  is a more appropriate indicator than is  $Ri_v$  of the extent of restratification achieved by this instability mechanism.

More compelling evidence for the inertial oscillation is presented in Fig. 10; see, in particular, the time evolution of the perturbation potential energy  $PE'$ , advection of perturbation potential energy ADV, and down- and cross-front perturbation kinetic energies  $KE'_{\parallel}$  and  $KE'_{\perp}$ . These results were obtained by running the  $Ri_v = 0.5$  simulation to a physical time that is unrealistically long in view of the time-independent forcing conditions and suppression of down-front variability. The effects of eddy diffusion also seem exaggerated over this longer time scale, as the inertial oscillation is more strongly damped than might be expected in reality. Note that from  $t \approx 200$  to  $t \approx 500$  the (nonmonotonic) decrease in the *magnitude* of  $PE'$  is also attributable to exaggerated eddy diffusion in combination with the specification of fixed-flux thermal boundary conditions; that is, with these boundary conditions and in the *absence* of convection and cross-front flow (for  $200 \leq t \leq 500$ ), it is readily shown that  $\theta \rightarrow 0$  as  $t \rightarrow \infty$  on a time scale  $O(\pi^2/Pe)$ . For weaker eddy diffusion of heat and momentum, however,

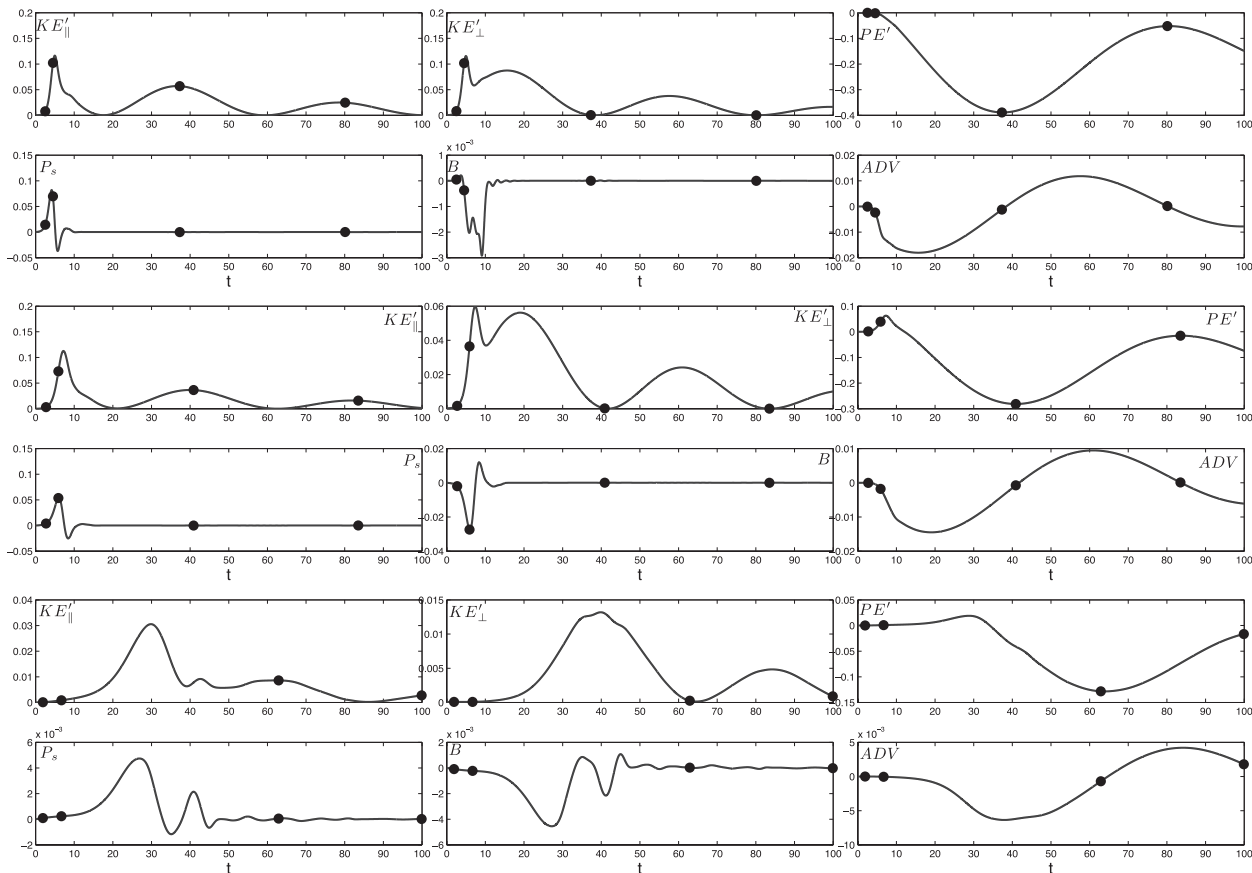


FIG. 9. Evolution of a subset of the various terms in the volume-averaged perturbation energy Eqs. (17), (18), and (19) for  $S = 1$ ,  $Ri_h = 0.15$ ,  $La = 0.001$ ,  $Pe = 4000$ , and (top)  $Ri_v = 0$ , (middle)  $Ri_v = 0.5$ , and (bottom)  $Ri_v = 1$ . “ADV” refers to the second term on the right-hand side of (19).

the diffusive relaxation of  $\bar{\theta}$  would be greatly slowed and the inertial oscillation presumably would continue nearly unabated, implying that  $\bar{\theta} < 0$  for all times of interest. Nevertheless, it is interesting to observe that the long-time dynamics for the *given* parameter regime apparently consists of intermittent bursts of convective activity, with amplification of residual hybrid LC/symmetric disturbances following nearly convection-free periods.

## 5. Conclusions

In this investigation, we have used a combination of linear stability theory and fully nonlinear numerical simulations to assess the influence of down-front-propagating surface waves on the evolution of submesoscale lateral fronts in the upper ocean. We briefly summarize our primary findings.

Through the action of the CL vortex force, surface waves fundamentally alter the linear stability of submesoscale fronts in (modified) thermal wind balance over

inertial time scales. Unlike classical symmetric instability modes, the hybrid Langmuir circulation/symmetric mode accomplishes significant *cross-isopycnal* transport. Over a wide parameter regime, surface waves are strongly destabilizing, leading to growth rates much larger than those exhibited by the classical symmetric mode. In fact, our linear analysis shows and nonlinear simulations confirm that the hybrid mode is operative for vertical Richardson numbers  $Ri_v \geq 1$ , while symmetric instability is completely suppressed in this regime.

Our numerical simulations also suggest that the nonlinear evolution of the hybrid mode can drive vertical restratification within the mixed layer. This restratification process is efficient in that it has been shown to occur on a time scale of less than one day—faster than the restratification accomplished by the 3D “mixed layer instabilities” (MLI) discussed by Boccaletti et al. (2007). The restratification is also potentially significant in that maximum vertical Brunt frequencies up to an order of magnitude larger than those associated with the base state, and approximately 4 times larger than are

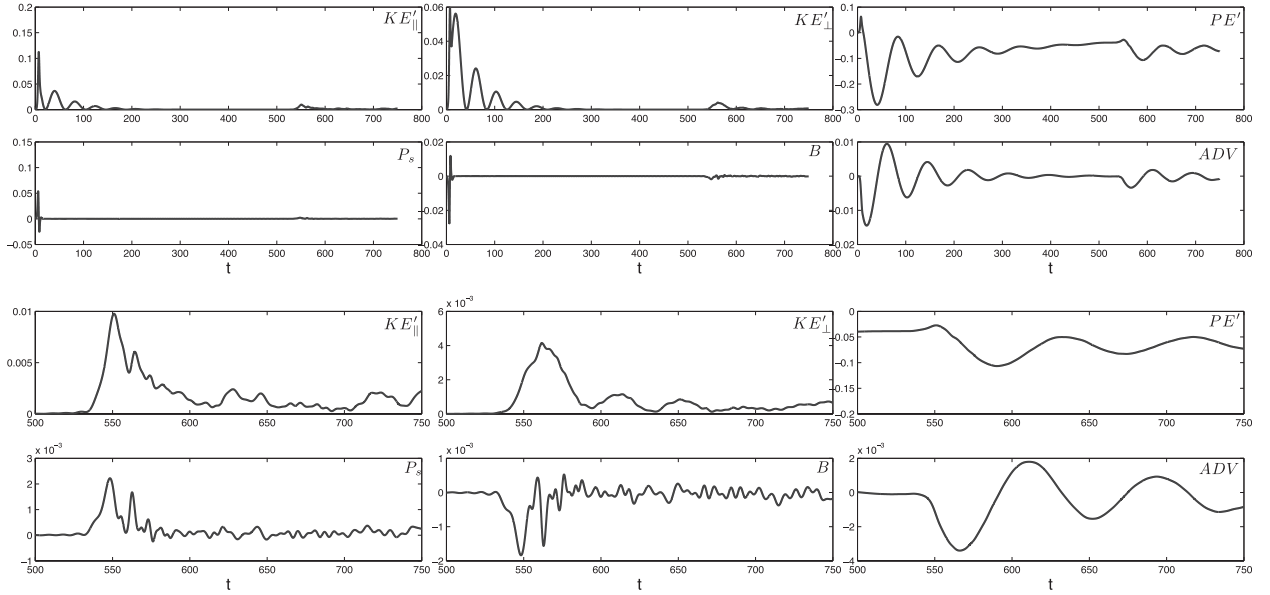


FIG. 10. Long-time evolution of various terms in the volume-averaged perturbation energy equations for  $S = 1$ ,  $Ri_h = 0.15$ ,  $La = 0.001$ ,  $Pe = 4000$ , and  $Ri_v = 0.5$ , corresponding to the middle panels in Fig. 9. (top) Evolution from  $t = 0$  to  $t = 750$ . (bottom) Close-up of evolution from  $t = 500$  to  $t = 750$ , when the hybrid instability is re-excited. Note that, except for a short transient near  $t = 0$ , the perturbation potential energy  $PE' < 0$ , indicating the occurrence of restratification. Moreover, the period of the slow oscillation in  $PE'$  is consistent with that of a damped inertial oscillation for the given parameters.

attainable by classical symmetric instability, can be achieved. The key physical mechanism at work in the restratification process is a cross-front shear flow, driven by a nonlinear interaction of the inclined and counter-rotating cells. Paradoxically, this result suggests that Langmuir circulation, which is generally viewed as a key vertical mixing mechanism within the upper ocean, may actually play a role in *supporting* vertical stratification.

Of course, these conclusions must be tempered by a number of factors. First, owing to Coriolis forces, the restratification is time-dependent. However, the *time-averaged* vertical stratification is indeed increased during the nonlinear stages of the instability. (For example, for  $Ri_v = 0$  and  $S = 1$ , the appropriately time-averaged  $N^2$  is roughly 2.7.) The crucial result of this investigation is that, in the presence of down-front-propagating

surface waves, some fraction of the potential energy stored in the front can be accessed by the hybrid instability mode and converted into mean kinetic energy. In the absence of dissipative and three-dimensional (3D) effects, the oscillation in the vertical stratification would presumably continue unabated. Of course, this assertion also presumes that there is strictly one-way coupling between the submesoscale front and the convective instabilities, and that various submesoscale external forcings remain fixed indefinitely, including those responsible for the occurrence or lack of dynamic buoyancy forcing via Ekman drift. Thus, two key questions to be addressed in future studies include the role of three-dimensionality—that is, both the 3D evolution of the hybrid instability and its possible interaction with other 3D frontal instabilities, particularly the baroclinic

TABLE 2.  $N_{\max}^2$  and  $N_{\min}^2$  for  $Ri_h = 0.15$ ,  $La = 0.001$ , and  $Pe = 4000$ .  $t_{\max}$  and  $t_{\min}$  correspond to the nondimensional times at which  $N_{\max}^2$  and  $N_{\min}^2$  are attained. Note that  $N^2(t = 0) = Ri_v$ .

$Ri_v$	$S$	$N_{\max}^2$	$t_{\max}$	$N_{\min}^2$	$t_{\min}$
0	0	1.4816	30.3	0.3443	51.5
0	1	4.0204	37.3	0.5782	80.7
0.5	0	0.8050	148.7	$\approx 0.75$	200
0.5	1	3.3897	40.9	0.6897	83.9
1	0	1	0	1	0
1	1	2.3265	62.9	1.1129	107.1

TABLE 3.  $(\Delta \bar{U})_{\min}^2$  and  $Ri_{v_{\max}}$  for  $Ri_h = 0.15$ ,  $La = 0.001$ , and  $Pe = 4000$ .  $t_{\min}$  and  $t_{\max}$  correspond to the nondimensional times at which  $\Delta U_{\min}$  and  $Ri_{v_{\max}}$  are attained.

$Ri_v$	$S$	$(\bar{U} _{z=0} - \bar{U} _{z=-1})_{\min}^2$	$t_{\min}$	$Ri_{v_{\max}}$	$t_{\max}$
0	0	0.2776	50.7	1.2744	49.1
0	1	0.1353	78.5	4.5668	75.7
0.5	0	0.9965	170.3	0.7821	163.5
0.5	1	0.2441	81.9	2.9641	78.3
1	0	1	0	1	0
1	1	0.5991	104.7	1.8892	100.9

TABLE 4. Definition of various terms in the volume integrated perturbation energy Eqs. (17)–(19).

$-D_{\parallel}$	$-\text{La}\langle \mathbf{V}u ^2\rangle$	Dissipation of $\text{KE}_{\parallel}$
$-D_{\perp}$	$-\text{La}\langle \mathbf{V}v ^2 +  \mathbf{V}w ^2\rangle$	Dissipation of $\text{KE}_{\perp}$
$B$	$+\text{Ri}_h\langle w\theta\rangle$	Buoyancy production
$C$	$-\text{Ro}^{-1}\langle uw\rangle$	Coriolis transfer
$P_S$	$-\left\langle uw \frac{dU_S}{dz} \right\rangle$	Stokes production
$P_U$	$-\left\langle uw \frac{dU_B}{dz} \right\rangle$	$x$ -shear production

MLIs—and the fully two-way coupling between submesoscale flows and convective instabilities, such as the hybrid mode studied here.

*Acknowledgments.* GPC gratefully acknowledges funding for this work from NSF CAREER Award 0348981, NSF CMG Award 0934827, and NASA ROSES08 NNX09AF38G subcontract. A portion of these funds was used to support KL and ZZ.

## REFERENCES

- Boccaletti, G., R. Ferrari, and B. Fox-Kemper, 2007: Mixed layer instabilities and restratification. *J. Phys. Oceanogr.*, **37**, 2228–2250.
- Craik, A. D. D., 1977: The generation of Langmuir circulations by an instability mechanism. *J. Fluid Mech.*, **81**, 209–223.
- , and S. Leibovich, 1976: A rational model for Langmuir circulations. *J. Fluid Mech.*, **73**, 401–426.
- Ferrari, R., and D. Rudnick, 2000: The thermocline structure of the upper ocean. *J. Geophys. Res.*, **105**, 16 857–16 883.
- Haine, T. W. N., and J. C. Marshall, 1998: Gravitational, symmetric, and baroclinic instability of the ocean mixed layer. *J. Phys. Oceanogr.*, **28**, 634–658.
- Holm, D. D., 1996: The ideal Craik-Leibovich equations. *Physica D*, **98**, 415–441.
- Hoskins, B. J., 1974: The role of potential vorticity in symmetric stability and instability. *Quart. J. Roy. Meteor. Soc.*, **100**, 480–482.
- Huang, N., 1979: On surface drift currents in the ocean. *J. Fluid Mech.*, **91**, 191–208.
- Leibovich, S., 1977: On the evolution of the system of wind drift currents and Langmuir circulations in the ocean. Part 1. Theory and averaged current. *J. Fluid Mech.*, **79**, 715–743.
- , 1983: The form and dynamics of Langmuir circulations. *Annu. Rev. Fluid Mech.*, **15**, 391–427.
- Lewis, D. M., and S. E. Belcher, 2004: Time-dependent, coupled, Ekman boundary layer solutions incorporating Stokes drift. *Dyn. Atmos. Oceans*, **37**, 313–351.
- Li, M., and C. Garrett, 1995: Is Langmuir circulation driven by surface waves or surface cooling? *J. Phys. Oceanogr.*, **25**, 64–76.
- , and —, 1997: Mixed layer deepening due to Langmuir circulation. *J. Phys. Oceanogr.*, **27**, 121–132.
- , —, and E. Skillingstad, 2005: A regime diagram for classifying turbulent large eddies in the upper ocean. *Deep-Sea Res. I*, **52**, 259–278.
- McWilliams, J. C., P. P. Sullivan, and C. Moeng, 1997: Langmuir turbulence in the ocean. *J. Fluid Mech.*, **334**, 1–30.
- Molemaker, M. J., J. C. McWilliams, and I. Yavneh, 2005: Baroclinic instability and loss of balance. *J. Phys. Oceanogr.*, **35**, 1505–1517.
- Munk, W., L. Armi, K. Fischer, and Z. Zachariasen, 2000: Spirals on the sea. *Proc. Roy. Soc. London*, **456A**, 1217–1280.
- Samelson, R. M., and C. A. Paulson, 1988: Towed thermistor chain observations of fronts in the subtropical north Pacific. *J. Geophys. Res.*, **93**, 2237–2246.
- Skillingstad, E. D., and D. W. Denbo, 1995: An ocean large-eddy simulation of Langmuir circulations and convection in the surface mixed layer. *J. Geophys. Res.*, **100**, 8501–8522.
- Stone, P., 1970: On non-geostrophic baroclinic instability: Part II. *J. Atmos. Sci.*, **27**, 721–727.
- Taylor, J., and R. Ferrari, 2009: On the equilibration of a symmetrically unstable front via a secondary shear instability. *J. Fluid Mech.*, **662**, 103–113.
- , and —, 2010: Buoyancy and wind-driven convection at mixed layer density fronts. *J. Phys. Oceanogr.*, **40**, 1222–1242.
- Thomas, L. N., and P. B. Rhines, 2002: Nonlinear stratified spin-up. *J. Fluid Mech.*, **473**, 211–244.
- , and R. Ferrari, 2008: Friction, frontogenesis, and the stratification of the surface mixed layer. *J. Phys. Oceanogr.*, **38**, 2501–2518.
- Thorpe, S. A., 2004: Langmuir Circulation. *Annu. Rev. Fluid Mech.*, **36**, 55–79.
- Trefethen, L. N., 2000: *Spectral Methods in Matlab*. SIAM, 184 pp.